Department of Physics and Astronomy
Heidelberg University

Bachelor Thesis in Physics
submitted by

Jonah Lux

born in Frankfurt am Main (Germany)

2024

Optimizing Stability in Accordion Lattice Dipole Trap through Piezoelectric Algorithmic Phase Correction

This Bachelor Thesis has been carried out by Jonah Lux at the
Physical Institute Heidelberg (PI)
under the supervision of
Prof. Dr. Lauriane Chomaz

Abstract

This thesis reports on the enhancement of the stability of an accordion lattice dipole trap by integrating an imaging setup and a feedback algorithm based on phase correction. After precise alignment an extraction of the phase through the relative positions of the middle interference fringe and the center of the Gaussian upper envelope was possible. Passive-stability measurements revealed a long-term phase drift of 0.6π over a 12-hour period. This would shift the 20 µm-sized fringe, planned to be used when loading the 3D atomic cloud into the accordion trap, by 5.81 µm, thus inducing atom loss while loading, as well as potential loading in two fringes. A piezo control setup successfully allowed manipulation of the phase via voltage application. The developed feedback algorithm automated the phase measurement and analysis, as well as the calculation and application of the necessary voltage correction. The final configuration results in an average phase deviation of 0.085π, corresponding to a center fringe displacement of 0.83 µm while loading and a reduction in the trap depth of 0.056%. Further limiting the phase fluctuation leads to increasing instabilities due to a lack of correction accuracy. The corresponding standard deviation of 0.054π shows the limitation of the setup. Novel piezo and mirror mounting as well as the transition to the main setup is expected to improve the operation of the feedback algorithm and yield a reduction of the phase deviation.

Kurzfassung

Diese Arbeit berichtet von der Stabilitätsverbesserung einer Akkordeon-Gitter-Dipolfalle durch die Integration eines bildgebenden Aufbaus und eines auf Phasenkorrektur basierenden Feedback-Algorithmus. Nach präziser Einstellung war eine Extraktion der Phase durch die relativen Positionen des mittleren Interferenzstreifens und des Zentrums der oberen Gaußschen Einhüllenden (erhalten durch einen Fit) möglich. Passive Stabilitätsmessungen ergaben einen Phasendrift von $0{,}6\pi$ über einen Zeitraum von 12 Stunden. Dies würde eine Verschiebung des 20 µm großen Streifens, der beim Laden der 3D-Atomwolke in die Akkordeonfalle verwendet wird, um 5.81 µm bedeuten. Dadurch kommt es zu Atomverlusten während des Ladens sowie zu einer potenziellen Beladung in zwei Streifen. Ein Piezo-Kontrollsystem ermöglichte die erfolgreiche Manipulation der Phase durch Anlegen einer Spannung. Der entwickelte Feedback-Algorithmus automatisiert die Phasenmessung und -analyse sowie die Berechnung und Anwendung der erforderlichen Spannungskorrektur. Die endgültige Konfiguration ergibt eine durchschnittliche Phasenabweichung von $0{,}085\pi$, was einer Verschiebung des mittleren Streifens um 0.83 µm während des Ladens und einer Verringerung der Fallentiefe von 0,056% entspricht. Eine weitere Begrenzung der Phasenfluktuation führt aufgrund mangelnder Korrekturgenauigkeit zu zunehmenden Instabilitäten. Die entsprechende Standardabweichung von $0{,}054\pi$ zeigt die Grenzen dieses Aufbaus auf. Es wird erwartet, dass eine neuartige Piezo- und Spiegelmontage sowie der Einbau in das Hauptexperiment die Funktionsweise des Feedback-Algorithmus verbessern und eine Verringerung der Phasenabweichung bewirken.

Contents

1 Introduction

The discovery of quantum physics was a significant turning point in modern physics history and has greatly influenced our current worldview. A significant contribution to this was made by the indian physicist Satyendra Nath Bose, particularly through his work on the quantum statistics of photons. This work was taken up by Albert Einstein, who further developed it by applying the derived principles to atoms. In the course of this, he achieved the first theoretical prediction of an ultracold quantum state of indistinguishable bosons, later known as the Bose-Einstein condensate. Although the discoverer was initially sceptical about this prediction, finding it paradoxical and seemingly impractical, the first experimental realisations took place 70 years later at JILA [1] and MIT [2] and were rewarded with the Nobel Prize in Physics. Since then, the exploration of these BECs has paved the way for numerous significant contributions to the field of quantum physics, enabling a multitude of discoveries.

The Quantum Fluids Group in Heidelberg, works with a Dysprosium BEC, which, due to the large magnetic dipole moment of dysprosium, exhibits strong interatomic dipole-dipole interactions. These long range interactions in combination with the usual short range contact interaction, introduce intriguing new dynamics into the realm of ultracold gases and have led to several interesting discoveries in recent years. In the setup an innovative combination of magneto-optical traps and optical traps are used for probing atomic gases, allowing for precise control in a compact design. To further investigate the dynamics of the quantum system, the group is actively engaged in the development of an optical accordion lattice trap, which is designed to facilitate controlled two-dimensional confinement, thereby enhancing the ability to probe and analyze quantum gases.

The topic of this thesis is the stabilisation of the accordion lattice trap, by adding a Kepler configuration telescope to image the interference pattern and implementing a feedback loop controlling the phase via a piezo stack.

1.1 Bose-Einstein Condensate

The Bose-Einstein Condensate is a state of many indistinguishable bosons, in which a macroscopic number occupies the groundstate. This is possible because bosons follow the Bose-Einstein statistics. The average number of particles in the i-th quantum state is accordingly given by:

$$n_i = \frac{1}{e^{(\frac{E_i-\mu}{kT})} - 1} \tag{1.1}$$

The condensate develops below a temperature near absolute zero, when the thermal deBroglie wavelength λ_{dB} becomes larger than the mean spacing between the atoms, in other words the atomic wavepackets begin to "overlap". This takes place at a phase-space density of $\rho_{ps} = n\lambda^3 \simeq 2.612$ [3].
Reaching the so-called critical temperature, which at densities of $\sim 10^{18}$-$10^{20}\,\mathrm{m}^{-3}$ lies around 100-200 nK (there are some exceptions like Helium), led to the development of several cooling techniques such as laser cooling and evaporative cooling to reach this ultra cold regime. A fine spatial confinement implemented with magnetic or optical traps is also required in order to achieve the corresponding high phase-space density.
The introduction of innovative methodologies, exemplified by the optical dipole trap, alongside strategies aimed at reducing the dimensionality of quantum gases, has paved the way for the exploration of novel phenomena. Although Bose-Einstein condensation (BEC) typically arises in non-interacting systems, the intentional reduction of dimensionality seeks to amplify interactions and correlations, thereby emphasizing the complex interplay of quantum phenomena.

1.2 Dysprosium Quantum Gas

A species of BEC atoms with particularly intriguing properties is dysprosium, the species that possesses the largest magnetic moment among all elements in the periodic table. This implies, that in addition to the typically prevalent contact interactions in ultracold gases, dipole-dipole interactions now play a crucial role in shaping both the equilibrium properties and dynamics of the system.
Dysprosium belongs to the lanthanide family and was first identified in 1886 by the french chemist Paul Émile Lecoq de Boisbaudran, who first achieved the difficult process of isolating it from Holmium. It has an atomic Number of $Z = 66$ and is naturally composed of its seven stable isotopes [4], which are listed in table 1.1. The presence of four isotopes exhibiting comparable natural abundances holds significant scientific merit within the realm of cold atoms. This characteristic facilitates the examination of diverse systems, including Bose gases, Fermi gases, mixtures, and others, employing a consistent experimental configuration. In this experiment we will primarily concentrate on samples of ^{164}Dy.

Isotope	^{156}Dy	^{158}Dy	^{160}Dy	^{161}Dy	^{162}Dy	^{163}Dy	^{164}Dy
Natural Abundance	0.06%	0.1%	0.23%	18.9%	25.5%	24.9%	28.3%
Quantum Statistics	boson	boson	boson	fermion	boson	fermion	boson

Table 1.1: Stable isotopes of Dysprosium

The elctronic configuration of Dysprosium in its groundstate is given by

$$[1s^2 2s^2 2p^6 3s^2 3p^6 3d^{10} 4s^2 4p^6 4d^{10} 5s^2 5p^6]_{Xe} 4f^{10} 6s^2. \tag{1.2}$$

Here we see that only the $4f$-shell is not fully occupied and its four unpaired electrons are therefore the sole source of angular momentum. They result in an orbital angular momentum of $L = 6$, a spin of $S = 2$ and due to LS-Coupling a total angular momentum of $J = L + S = 8$. Accordingly, the ground state of Dysprosium can be written as ${}^5I_8$. This also results in the large magnetic moment of $\mu \sim 10\mu_B$, which induces the dipolar interactions.
Surrounding this unfilled $4f$-shell is a filled $6s$-shell, whose electrons are used to cool and trap the Dysprosium atoms, the two electronic transitions are shown in figure 1.1.

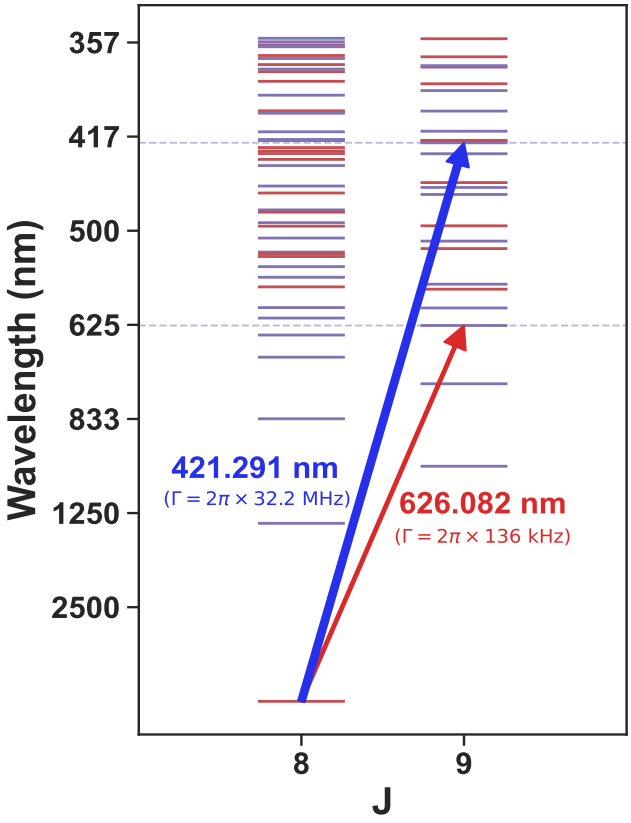

Figure 1.1: Energy level diagram of dysprosium for the levels of total electronic angular-momentum quantum number J = 8 and J = 9. The color of the energy states indicate their parity, where red relates to even and blue to odd parity. The used transitions are indicated with arrows, where the thickness of the arrows corresponds to their linewidths. Taken from [5].

1.3 The Dylab

This section gives a short overview of the Dysprosium experiment in Heidelberg, a schematic drawing of the setup is shown in figure 1.2. To first generate a thermal gas of dysprosium atoms, solid dysprosium is heated to about 1000°C in an high-temperature effusion oven. From there, the atoms exit with a mean velocity of around 400 m/s, entering a vertically mounted two-dimensional magneto-optical trap (2D MOT), designed to cool the gas and confine it in the $x - z$ plane [6]. Its octagonal chamber consists of six viewports for optical access. Four of those are used by the 421nm trapping laser beams in a bow-tie $\sigma_+\sigma_-$ retroflected configuration [5]. Eight blocks of permanent magnets create the gradient magnetic field inducing the spatially-varying Zeeman shift.

After this first cooling stage, the slowed atoms are pushed in y-direction by a push beam, entering the science chamber. The heart of this chamber forms a 3D

MOT, comprised of one conventional and two orthogonal retro-reflected 626nm laser beams, as well as a pair of magnetic coils in anti-Helmholtz configuration along the z-axis, creating a quadrupole field. Additionally, the chamber contains another pair of coils generating a homogeneous field along the z-axis, as well as two pairs of rectangular coils surrounding it and producing a homogeneous field in x- and y-direction. For further details see [7] and [8]. Subsequently, the atoms are loaded into an optical dipole trap (ODT), since the MOT is not capable of reaching the required temperatures to form a BEC. The ODT consists of two crossed laser beams with a wavelength of 1064nm, far away from resonance. Here, the method of evaporative cooling is used, in which the most energetic atoms are removed from the trap, by lowering the depth of the trapping potential step-by-step. After each step, a new reduced thermal equilibrium emerges, due to inter-particle interactions, again forming an energy-distribution with a high energetic tail which can escape in the next step. This reduces the overall temperature of our system, enabling it to reach the BEC regime.
After achieving quantum degeneracy, the aim is to tightly confine the atomic cloud in one dimension, creating a quasi 2D-gas. To realize that compression, the implementation of an optical lattice trap with configurable periodicity, a so-called accordion lattice, is planned. The stability optimization of this trap will be the topic of this thesis. For a more detailed characterization of the design and implementation of the accordion lattice refer to [9] and [10]. Additionally, a Digital Micromirror Device (DMD) for generating versatile trapping potentials is in progress.

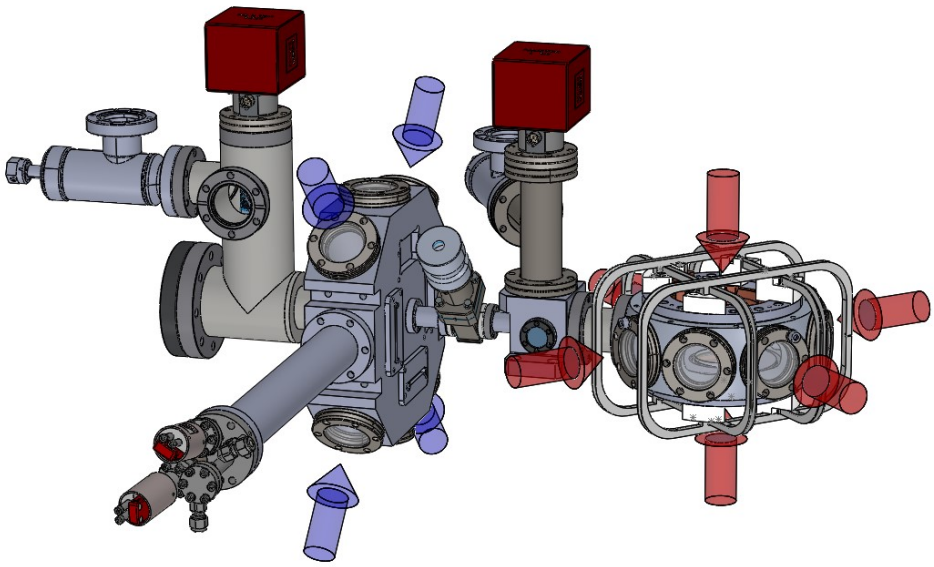

Figure 1.2: Sketch of the experimental setup: Atoms emitted from the high-temperature oven's hot jet are first trapped in the 421 nm 2D-MOT (indicated by blue arrows), then directed into the main chamber where they undergo capture once more in the 626 nm 3D-MOT (illustrated by red arrows). Subsequently, the atoms are loaded into a 1064 nm optical dipole trap, initiating evaporative cooling to achieve the BEC regime. Taken from [11].

2 Fundamentals

This chapter introduces the main ideas and models necessary to understand and describe the physics behind trapping with an accordion lattice. A short explanation of the essential concepts of optical dipole trapping, as well as two-dimensional trapping will be given, followed by a theoretic description of the accordion lattice's characteristics.

2.1 Optical Dipole Trapping

Optical dipole trapping is a powerful technique in the field of atomic and molecular physics, as well as in quantum optics. This method is based on the concept of dipole moments induced in neutral atoms or molecules by the presence of an external electric field, such as that generated by laser beams. To explain the basic theoretical principles the following section on the trapping of neutral atoms is based on the 1999 Review by Grimm, Weidemüller and Ovchinnikov [12].

2.1.1 Trapping of Neutral Atoms

When an atom is situated in a monochromatic laser, it experiences an electric field

$$\mathbf{E}(\mathbf{r},t) = \hat{\mathbf{e}}\tilde{E}(\mathbf{r})\exp(-i\omega t) + \text{c.c.} \tag{2.1}$$

which induces a dipole moment

$$\mathbf{p}(\mathbf{r},t) = \hat{\mathbf{e}}\tilde{p}(\mathbf{r})\exp(-i\omega t) + \text{c.c.} \tag{2.2}$$

oscillating with the excitation frequency ω, $\hat{\mathbf{e}}$ being the unit polarization vector. The amplitude $\tilde{p}$ of the dipole moment is proportional to the field amplitude $\tilde{E}$ by the factor α, which represents the complex polarizability.

$$\tilde{p} = \alpha\tilde{E} \tag{2.3}$$

The resulting atom-light interaction potential is then given by:

$$V_{\text{dip}} = -\frac{1}{2}\hbar\langle \mathbf{p}\cdot\mathbf{E}\rangle = -\frac{1}{2}\frac{\hbar}{\varepsilon_0 c}\text{Re}(\alpha)I, \tag{2.4}$$

with the field intensity $I = 2\varepsilon_0 c|\tilde{\mathbf{E}}|^2$ and taking into consideration that the dipole moment is induced rather than permanent, the factor of $1/2$ is introduced. The gradient of this potential result in the conservative dipole force

$$\mathbf{F}_{\text{dip}}(\mathbf{r}) = -\nabla U_{\text{dip}}(\mathbf{r}) = \frac{1}{2\varepsilon_0 c}\text{Re}(\alpha)\nabla I(\mathbf{r}). \tag{2.5}$$

The scattering rate Γ_{sc} is described as the ratio of power absorbed by the oscillator from the driving field P_{abs} and the photon energy $\hbar\omega$:

$$P_{\text{abs}} = \langle \dot{\mathbf{p}}\mathbf{E}\rangle = \frac{\omega}{\varepsilon_0 c}\text{Im}(\alpha)I \tag{2.6}$$

$$\Gamma_{\text{sca}} = \frac{P_{\text{abs}}}{\hbar\omega} = \frac{1}{\hbar\varepsilon_0 c}\text{Im}(\alpha)I(r) \tag{2.7}$$

To compute the polarizability α, an electron that is elastically bound to the core with an oscillation eigenfrequency ω_0 corresponding to the optical transition frequency is considered. This gives the following expression for the polarizability

$$\alpha = 6\pi\varepsilon_0 c^3 \frac{\Gamma/\omega_0^2}{\omega_0^2 - \omega^2 - i\left(\frac{\omega^3}{\omega_0^2}\right)\Gamma}, \tag{2.8}$$

which is valid for far-detuned, low saturated light with very low scattering rates ($\Gamma_{sca} \ll \Gamma$). Here Γ describes the on-resonance damping rate resulting from the dipole radiation of the oscillating electron:

$$\Gamma = \left(\frac{\omega_0}{\omega}\right)^2 \frac{e^2\omega^2}{6\pi\varepsilon_0 m_e c^3} \tag{2.9}$$

Using the rotating wave approximation, the dipole potential and scattering rate simplify to:

$$V_{\text{dip}}(\mathbf{r}) = \frac{3\pi c^2}{2\omega_0^3}\frac{\Gamma}{\Delta}I(\mathbf{r}), \tag{2.10}$$

$$\Gamma_{\text{sc}}(\mathbf{r}) = \frac{3\pi c^2}{2\hbar\omega_0^3}\left(\frac{\Gamma}{\Delta}\right)^2 I(\mathbf{r}). \tag{2.11}$$

with $\Delta = \omega - \omega_0$. This implies that operating below an atomic resonance ($\Delta < 0$), called *red detuning*, the dipole potential becomes negative, leading to an attractive interaction that draws atoms into the light field. Consequently, potential minima are located at positions characterized by maximum intensity. Conversely, above resonance ($\Delta > 0$), called *blue detuning*, the dipole interaction repels atoms away from the field, causing potential minima to align with intensity minima. Furthermore it is evident, that the scaling of the dipole potential involves a proportionality to I/Δ, while the scattering rate has a scaling of I/Δ^2, which is the reason most optical dipole traps commonly employ significant detunings and high intensities to minimize the scattering rate.

2.1.2 Polarizability of Dysprosium

As will be demonstrated in section 2.3, the complex polarizability is required to determine the depth of our trap, necessitating a precise quantification. However, for dysprosium, equation 2.8 to calculate the scalar polarizability is insufficient, and both the vectorial and the tensorial polarizability must be additionally taken into account. Theoretical simulations [13] and extensive experimental measurements [14] were conducted for determination. For the chosen wavelength of 532 nm experimental results yield a range of (64-386) *a.u.* [15], as well as an estimation of 10.5 *a.u.* [16]. The theoretical value which will be used for calculations in this thesis is 350 *a.u.* [17].

2.2 Two-Dimensional Trapping

The physics of a quantum gas strongly depend on the dimensionality of the system. By tightly trapping the atoms in one direction and therefore limiting the motion of the gas, one can reduce its dimensions to a 2D-plane. Here we require a very anisotropic potential with $\omega_z \gg w_{perp}$ and a supression of thermal- and interaction-induced excitations into the excited transverse modes [18]:

$$\hbar\omega_z \gg k_B T, \mu, \tag{2.12}$$

with μ being the chemical potential induced by interatomic repulsive interactions and T the temperature of the trapped particles. One frequently applied technique to fulfill these requirements is the **accordion lattice**, which provides precise control over the traps geometry and size.

2.3 The Accordion Lattice

The idea of an optical lattice with variable periodicity to confine an atomic cloud in one direction was first achieved in 2008 by Li, Kelkar, Medellin, and Raizen at the University of Texas [13] and since then implemented in many experiments. The general design is depicted in figure 2.1 and consists of two laser beams, which intersect at an angle of 2θ, creating a one-dimensional interference pattern. By adjusting the beam intersection angle, the fringe size of the pattern can be controlled, allowing convenient atom loading at large periods, subsequently compressing the cloud by decreasing the period.

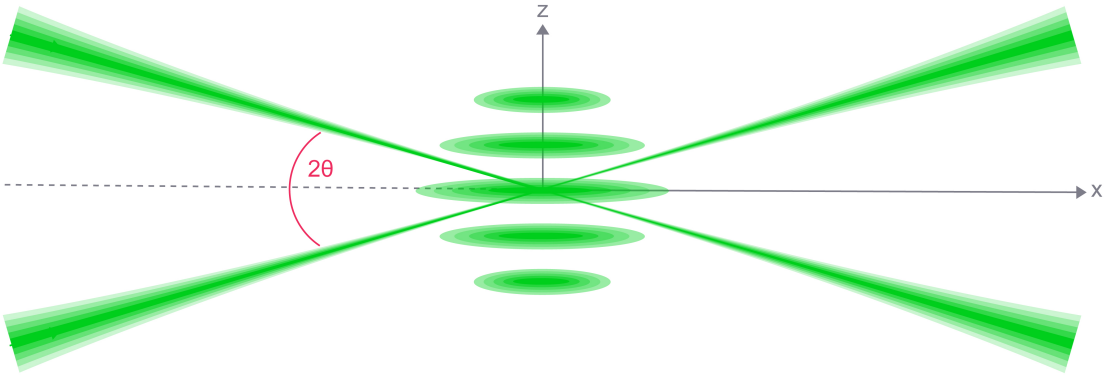

Figure 2.1: Working principle of an accordion lattice. Two laser beams are made to intersect at an angle, producing a one-dimensional interference pattern. Taken from [9].

In most cases, the two intersecting beams have a Gaussian shape and should ideally be identical. The electric field of a Gaussian beam propagating in the x-direction is given by:

$$\mathbf{E}(r,x) = E_0\hat{\mathbf{x}}\frac{w_0}{w(x)}\exp\left(-\frac{r^2}{w(x)^2}\right)\exp\left(-i\left(kx + k\frac{r^2}{2R(x)} - \psi(x)\right)\right) \tag{2.13}$$

where:

$\mathbf{E}(r, x)$ is the electric field amplitude at position (r, x),
r is the radial distance from the center axis of the beam,
z is the axial distance from the beam waist,
E_0 is the peak electric field amplitude,
$w(x)$ is the beam waist radius at position x,
k is the wave number of the light,
$R(x)$ is the radius of curvature of the wavefronts at position x,
$\psi(x)$ is the Gouy phase shift at position x.

The beam waist w_0 and Rayleigh range z_R are related to the parameters of the beam as follows:

$$w_0 = w(0), \tag{2.14}$$

$$z_R = \frac{\pi w_0^2}{\lambda}. \tag{2.15}$$

If these beams are now deflected by $\pm\theta$ from the x-axis, as seen in figure 2.1, with corresponding electric fields $\mathbf{E}_\theta$ and $\mathbf{E}_{-\theta}$,the following equation describes the intensity of the resulting interference pattern:

$$I_{\text{tot}}(x, y, z) = |\mathbf{E}_\theta + \mathbf{E}_{-\theta}|^2 \tag{2.16}$$

$$= |\mathbf{E}_\theta|^2 + |\mathbf{E}_{-\theta}|^2 + \mathbf{E}_\theta^* \mathbf{E}_{-\theta} + \mathbf{E}_\theta \mathbf{E}_{-\theta}^* \tag{2.17}$$

For equal linear polarizations this yields [9]:

$$I_{\text{tot}}(x, y, z) = I_\theta + I_{-\theta} + 2\sqrt{I_\theta}\sqrt{I_{-\theta}} \cdot \cos\left(\frac{2\pi}{d} z + \Delta\varphi\right) \tag{2.18}$$

with $I_{\pm\theta}$ being the intensities of the two individual Gaussian beams

$$I_\theta(x,y,z) = \frac{2P}{\pi w_y(x_\theta) w_z(x_\theta)} \exp\left(-\frac{2y^2}{w_y^2(x_\theta)} - \frac{2(z\cos(\theta) + x\sin(\theta))^2}{w_z^2(x_\theta)}\right) \quad (2.19)$$

$$I_{-\theta}(x,y,z) = \frac{2P}{\pi w_y(x_{-\theta}) w_z(x_{-\theta})} \exp\left(-\frac{2y^2}{w_y^2(x_{-\theta})} - \frac{2(z\cos(\theta) - x\sin(\theta))^2}{w_z^2(x_{-\theta})}\right) \quad (2.20)$$

with $\Delta\varphi = \varphi_\theta - \varphi_{-\theta}$ representing the phase difference between, the beam waists w_z and w_y and the power P of each beam.

Generally speaking, for the plane transverse to the beams' propagation, the shape of the total intensity I_{tot} is therefore defined by an interference sinusoid contained within an upper and a lower envelope of approximate Gaussian shape (see figure 2.2). The exact solution of the two envelopes is given by the superposition of the two Gaussian terms (equation 2.19 and 2.20). For perfectly overlapping beam centers and equal amplitudes, this results in a single Gaussian upper envelope, while the lower envelope cancels two zero, as depicted in figure 2.2a. For unequal amplitudes, the lower envelope also takes the form of a Gaussian with the magnitude depending on the amplitude difference. For slight misalignments of the two beam centers, an additional shift of the lower envelope occurs. In this case both envelopes still have the approximate shape of a single Gaussian distribution, as shown in figure 2.2b. This is the scenario we use for fitting (see section 4.1.1).

For severe misalignments this approximation of single Gaussians is not valid anymore and a superposition of the individual beams has to be calculated.

Figure 2.3 represents the ideal trapping potential, which, in this case of red detuning, becomes minimal at the point of maximum intensity and can be described in general by the following equation:

$$U(x,y,z) = \frac{I_{\text{tot}}(x,y,z)\alpha}{2c\epsilon_0}. \quad (2.21)$$

Also employed here is the following definition of the spacing between two minima, so-called fringes:

$$d = \frac{\lambda}{2\sin(\theta)}. \quad (2.22)$$

For $\Delta\varphi = 0$ the center of the envelope and the center of the middle fringe overlap, for a phase difference $\Delta\varphi \neq 0$ the distance between these two centers amounts to

$$l = \frac{\Delta\varphi}{2\pi} d. \tag{2.23}$$

To maximize the trapping potential, ideally, this distance should be zero. Achieving this consistently through active regulation of $\Delta\varphi$ is the aim of this work.

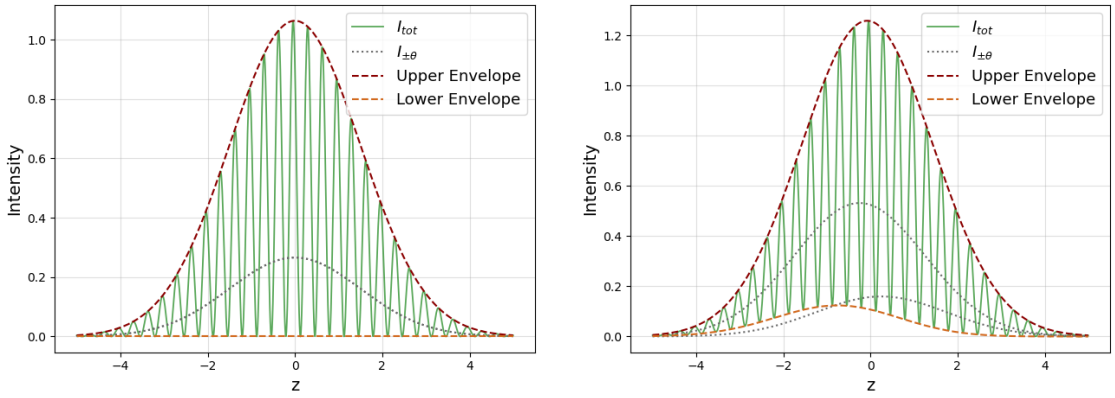

(a) Ideal Gaussian-sinusoid intensity distribution.

(b) Intensity distribution for unequal amplitudes and misaligned center positions.

Figure 2.2: Intensity distributions for different scenarios (arbitrary units).

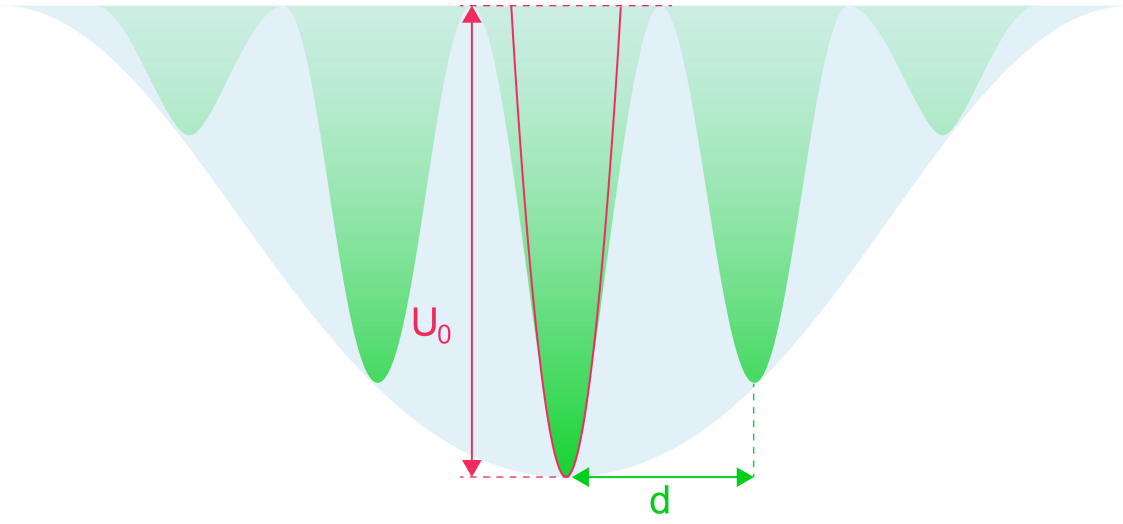

Figure 2.3: Trapping potential of the accordion lattice in the case of red detuning, with a second-order polynomial fitted to an individual fringe marked in red. Taken from [9].

3 Experimental Setup

The experimental setup for the accordion lattice is based on a previously designed configuration by Valentina Salazar Silva [9] and has been replicated in the scope of this work, as the intention is to integrate the original into the main experiment. Subsequently, the key features of this setup will be briefly elucidated, with detailed attention given to the imaging and stabilization setups added within the scope of this work.

3.1 Characterisation of the Accordion Lattice

3.1.1 Interference Pattern

To produce the above described interference pattern, a convex lens is used to intersect two initially parallel laser beams in its focal plane, as shown in figure 3.1. In this configuration the angle θ is defined by

$$\theta = \arctan\left(\frac{D}{2f}\right), \tag{3.1}$$

containing the focal length f and the distance between the parallel beams D. Due to the size of the viewport into the science chamber, the maximal possible interference angle is $\theta_{max} = 8.976°$. An angle close to this maximal value is needed to achieve the high vertical trapping frequencies of around 15 kHz required to reach the deep quasi 2D-regime. The minimal interference angle is determined by the requirement to load the entire atomic cloud into one fringe, resulting in a maximal fringe size of 20 µm and therefore a minimal angle of $\theta_{min} = 0.76°$ [9]. To fulfill these specifications a custom made high-precision aspherical lens with $f = 150\,\text{mm}$ was designed to minimize the aberrations in that range, which would have led to shifts of the interfering point, causing instabilities. For alignment purposes it is placed on a four-axis alignment stage.

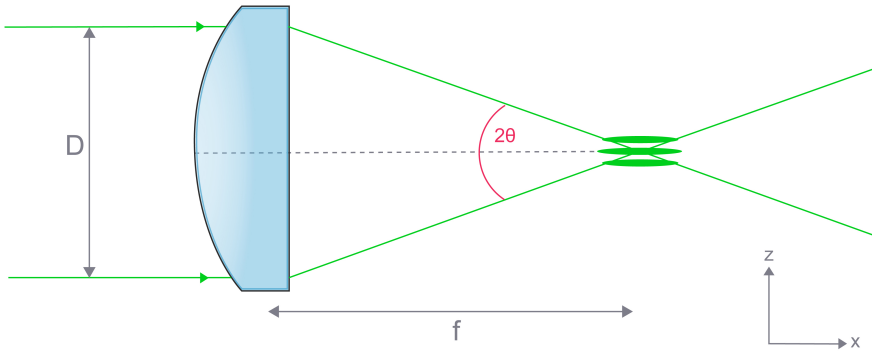

Figure 3.1: Experimental realization of the interference pattern with a convex lens. Taken from [9].

3.1.2 Beam-Separation Setup

The two laser beams entering the focusing lens should ideally be perfectly parallel and exact copies of each others. There are multiple successfully implemented methods that achieve this [13] [19] [20], the one used in this setup is depicted in figure 3.2a.
First, one beam is split in its s- and p-polarized component via a polarizing beam-splitter cube (PBS). The s-polarized part is reflected 90° away from the cube, where it is reflected again by a mirror. On its way back and forth it passes a quarter-wave plate twice, inducing a p-polarization. This allows the beam to now be transmitted through the PBS in direction of the lens. The p-polarized part is solely reflected by a 45° mirror directly towards the focusing lens, making it parallel to the lower beam. The whole beam separation setup is located on the upper part in a custom designed tower mount shown in figure 3.2b.
Due to misalignments in the polarization process the amplitude of the lower beam is around seven times larger than the one of the upper beam, as shown in figure 3.3.

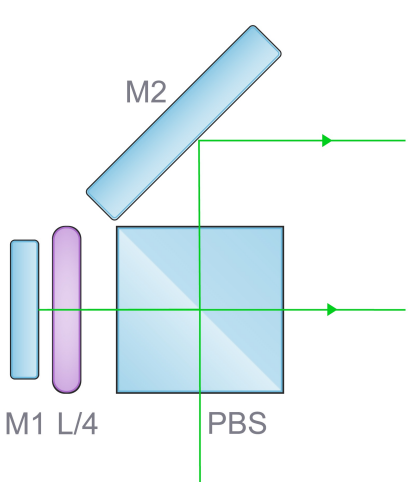

(a) Schematic overview of the beamsplitting.

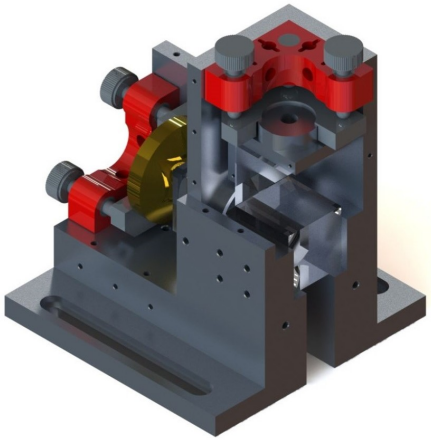

(b) Realisation of the beamsplitting with a custom designed tower.

Figure 3.2: Beamsplitting procedure, adapted from [9].

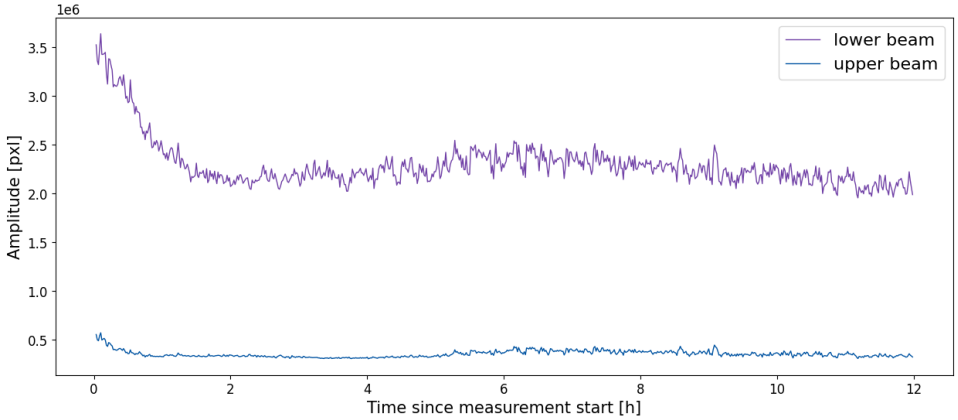

Figure 3.3: Comparison of the beam amplitudes.

3.1.3 Fringe-size Control

One of the main features of the accordion lattice is its ability to dynamically adjust the fringe size. This can be realised by mounting the 45° mirror directing the beam vertically to the tower mount on the upper level, on a linear horizontal translation stage. In the setup that is planned to be integrated in the main setup, this translation stage is motorized. Since a detailed analysis on the stability during compression using this stage has already been conducted [10], the novel test setup implemented here only uses a manual stage, which after a quick check for proper functioning was set on a fixed point. The final parameter implemented are shown in table 3.1.

Beam Distance D	Fringe Size d	Fringe Size (imaging plane)	Angle θ
17.5 mm	4.56 µm	201.76 µm	3.34°

Table 3.1: Final accordion lattice parameters

3.1.4 Beam Properties

In order to achieve sufficiently high trapping frequencies in the vertical plane while roughly maintaining symmetry in the residual plane as well as a large fringe intensity ratio, a wavelength of $\lambda = 532\,\text{nm}$ and beam waists of $w_z = 56.5\,\mu\text{m}$ and $w_y = 240\,\mu\text{m}$ are used. They vary slightly from the chosen optimal parameters, which were calculated in more detail by Valentina Salazar Silva [9]. To implement these parameters for an incoming beam with $\omega_0 = 500\,\mu\text{m}$, a set of two cylindrical lenses with $f_1 = 200\,\text{mm}$ and $f_1 = 150\,\text{mm}$ are used. Additionally, the setup consist of a half-wave plate and a PBS after the outcoupler for cleaning the polarization, as well as another half-wave plate behind the second lens, which controls the polarization of the beam and therefore the intensity ratio of the two interfering beams.

3.2 Controlling the Fringe Position

As explained in section 2.3, the primary goal of this thesis is to overlap the center position of the gaussian envelope with the middle fringe of the interference pattern, in order to maximize the trapping potential. Previous tests showed that significant phase drifts in the order of $\sim$7-12π can be observed [10], demonstrating that additional stabilisation is needed. The position of the center fringe is determined by the relative phase between the two interfering beams, which arises from the difference in path length. So, in order to control the relative phase and therefore the position of the center fringe, it is sufficient to manipulate the length for one of the beams' path. To achieve that, a piezoelectric transducer (Piezomechanik HPCh 150) is glued to the back mirror in the mount, which reflects the lower beam. Due to the piezoelectric effect it expands over microscopic distances when a voltage is applied, allowing for precise changes to the path length by increasing or decreasing the voltage. To know how much voltage needs to be applied, an imaging setup is required to extract the phase information and convert it into an output signal. This setup is explained in the next sections.

3.3 Fringe Imaging Setup

One of the main challenges for building the phase stabilisation setup, is the imaging to extract the phase information. Since in the final setup the interference pattern is located inside the high vacuum science chamber and populated by the cloud of cold atoms, the imaging system can not be placed directly at the pattern. Instead, two additional lenses are used as an optical Keplerian telescope to recreate the interference pattern, as well as a $\times 20$ objective lens for magnification. For capturing the final image, a WinCamD Beam-profile camera is used during the first part of this thesis, since its high resolution of 2048×2048 pixels with a pixel size of 5.5 µm was advantageous for aligning and testing the setup. For the final phase-stabilisation process, it is switched to a Mako G-234B CMOS camera with a resolution of 1936×1216 pixels and a pixel size of 5.86 µm, which due to the smaller sensor size had to be placed closer to the objective lens. The whole imaging setup is shown in figure 3.4. The second lens, employed to render the beams parallel again, is identical to the one used for focusing, thus also custom made with $f = 150$ mm. It is placed on a five-axis alignment stage at a distance of 30 mm from the first lens. In order to accurately recreate the interference pattern, the two lenses have to be aligned very precisely. The corresponding alignment procedure to reproduce two parallel beams is described in detail in the following section.

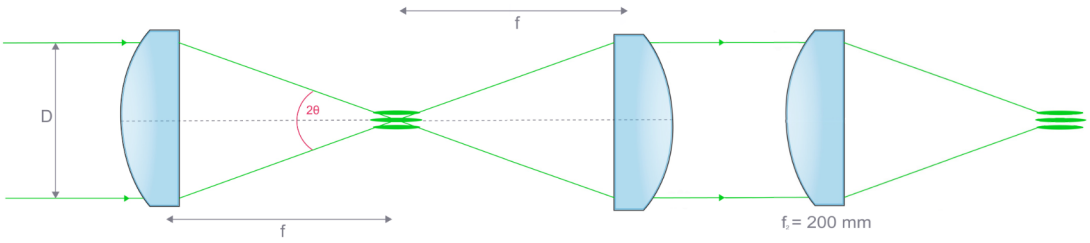

Figure 3.4: Telescope setup used to image the interference pattern. Adapted from [9].

3.3.1 Alignment Protocol

1. Bottom Setup
The alignment procedure begins by utilizing the beam profile camera alongside retro-reflection to align all waveplates and cylindrical lenses at the bottom layer. This initial step establishes a foundational alignment framework.

2. 45°-Mirror on the Translation Stage
The tower structure is mounted, and the cube is inserted, ensuring precise alignment of the 45°-mirror by utilizing the retro-reflection from the cube's surface. An alignment verification is conducted by examining the retro-reflection at the reflection branch of the cube, immediately after the fiber connection.

3. Back Mirror
The back mirror for the bottom beam is installed within the tower assembly. Without the presence of the quarter-waveplate, the beam is directed to reflect back. This reflection spot is aligned with the one established in the previous step, and their positions are denoted. Following this, a lens with a focal length approximately around 150 mm is inserted between the two cylindrical lenses to expand the beam size and facilitate observation of interference patterns. The position of the back mirror is adjusted to align the center of the interference rings with the marked position.

4. Quarter Waveplate
The "interference-lens" is removed, and the quarter-waveplate is inserted between the back mirror and the cube. A power meter is utilized to orient the quarter waveplate axis for minimal power in the transmitted portion following the cube.

5. Reference Mirror
A mirror is configured to reflect the bottom beam, ensuring adequate space above it to also reflect the upper beam post-installation of the top mirror. Ideally, the mirror is positioned far enough apart so that two lenses with a focal length of 150 mm each can fit between them (minimum distance of 40 mm). The reference mirror is aligned by superimposing the resulting interference rings at the reflection branch with the marked spot.

6. Top Mirror
The triangular top mirror is installed, and the center of the large interference ring aligns with the others, ensuring parallelism between the bottom and top beams.

7. Alignment of the Two Lenses

A) Test-Setup (Without Vacuum)

If not already completed, the reference mirror is relocated to allow space for both lenses and realigned for future reference. Another mirror is placed on a translation stage approximately at the focal position of the first lens and aligned accordingly. The first lens is installed, and the mirror is adjusted to the focal point, ensuring that the downward beam reflects upwards and vice versa. Alignment is verified by ensuring the overlap of the lower and upper beams at both positions in front of the mount, considering various translation stage positions. For increased precision, the lens between the two cylindrical lenses is employed to ideally observe large horizontal fringes. The second lens is then installed approximately 30 mm away from the first one and aligned by initially overlapping the reflections of both beams before the mount, followed by fine-tuning to superimpose all interference patterns at the marked spot.

B) Main Experiment (With Vacuum)

Due to space constraints within the science chamber, alignment of the second lens takes precedence. A mirror is placed on a translation stage at the approximate focal point of the second lens (around 45 mm from the position of the first lens) and aligned accordingly for future reference. The second lens is installed, and the translation stage is utilized to position the mirror precisely at the focal point, ensuring proper reflection of the downward beam upwards and vice versa. Alignment is confirmed by verifying the overlap of the lower and upper beams at both positions in front of the mount, considering various translation stage positions. The lens between the two cylindrical lenses is employed to observe large horizontal fringes for increased precision. Subsequently, the first lens is installed approximately 30 mm ahead of the second one and aligned by initially overlapping the reflections of both beams before the mount. Fine-tuning of the alignment is then conducted to superimpose all interference patterns at the marked spot.

3.4 Test-setup for Phase Stabilisation

The setup build for this thesis is a preliminary concept for testing the phase stabilisation process and feedback algorithm. Additional adjustments are necessary before implementation into the main experiment, like the integration to the existing labscript and control hardware.

The data captured by the camera is transmitted to a laptop, which uses an analysing script written in python to extract the distance between the middle fringe and the center of the gaussian envelope. If the fringe position needs correction, the distance is used to calculate the corresponding voltage needed for correction with the piezo-stack. Chapter 4 provides a detailed explanation of the extraction methods and feedback algorithm used. The laptop is connected to the wavefunction generator Siglent SDG6022X, and its output is connected to the analogue power amplifier, which is directly connected to the piezo-stack. The amplifier takes an input voltage of up to $\pm 5\,\mathrm{V}$ with additional options to set a fixed offset and an amplification. It ensures that the applied voltage does not damage the piezo by restricting the output voltage to a range of $-30\,\mathrm{V}$ to $150\,\mathrm{V}$. By applying the calculated DC-offset to the function generator, the voltage is amplified and passed to the piezo-stack, which induces a displacement of the fringes relative to the envelope.

4 Phase Stabilization

This chapter covers the realisation of the active phase stabilisation. A detailed description of the data analysis, a characterization of the piezoelectric control mechanism and a brief summary over the developed feedback algorithm will be given.

4.1 Data Analysis

In order to extract the essential information from the raw data captured by the camera, an analyzer script was written by Jianshun Gao, which will be briefly discussed in this section.

4.1.1 Fitting the data

To fit the data, the first step is rectifying the slight angular misalignment present in the captured images through straightforward rotation by eye, thereby enabling a more accurate analysis. Subsequent to this correction, the data, initially organized in a two-dimensional array, is summed along the x-axis and cut at the edges of the lattice, yielding a one-dimensional array whose shape is exemplified in figure 4.1.

As explained in more detail in section 2.3, a sinusoidal oscillation within a single Gaussian envelope is ideally expected, as evident in equation 2.18. However, a lower envelope with the shape of a Gaussian and a slight shift of its center relative to the upper envelope is observable. This is caused by the unequal beam amplitudes shown in figure 3.3, as well as a misalignment of the respective beam centers indicated by the center shift. Since both the shape of the lower and the upper envelope maintain a Gaussian shape, the misalignment is minor.
This confirms the precise alignment discussed in section 3.3.1 and allows a good approximation of the upper envelope using the fit of a single Gaussian. To fit the envelope, the data is normalized to one and a peakfinder is used to select the peaks maxima, with a minimum prominence of 0.05 to avoid noise-peaks. After

a predefined calculation of the starting parameters, the data is then fitted to the resulting dataset containing only the peaks.
To calculate a fit of the sinusoidal pattern, it is necessary to eliminate the lower envelope. This can be achieved by fitting the shape of the lower envelope, similar to the upper, but now using the minima of the normalized data and the superposition of two Gaussians. It is important to note that the starting parameters for this fit are very sensitive and need to be defined manually beforehand. Exemplerary fitting results are depicted in figure 4.2.
After subtracting the fitted curve from the dataset, a one-dimensional discrete Fourier transformation is performed using the Fast Fourier Transform (FFT) algorithm. The resulting frequency components are then filtered to remove low-frequency noise. By identifying the maximum frequency, the frequency of the interference peaks can be determined, which corresponds to the reciprocal of the fringe distance.
Finally, a fit model based on equation 2.18 is defined. This model utilizes the parameters computed in the previous fits, as well as the fringe distance, to calculate precise starting parameters. Since the model fits nine parameters, reliable starting values and well-chosen fit bounds are essential. The result of a successful fit will therefore be passed as starting parameters to the next fit. An exemplary fit, together with the upper and lower envelope, is illustrated in figure 4.2.

It is also evident in figure 4.1, that the data captured with the Mako camera shows noticeable discrepancies from the data captured with the WinCamD, as well as from the approximated Gaussian shape. This makes the fit less reliable and introduces a potential source of error. However, test measurements still show satisfactory results for fits applied to the data.

4.1.2 Extracting the Phase of the Interference Pattern

As a result of the fit exemplified in figure 4.2, one of the parameters obtained is the phase, which yields important information regarding the stability of the trap. However, since fitting all the data is time-consuming, we sought an alternative method to determine the phase. Equation 2.23 shows that it is also possible to calculate the phase using the distance between the middle fringe and the upper envelope or any other fixed point. A comparison between both methods is depicted in figure 4.3.

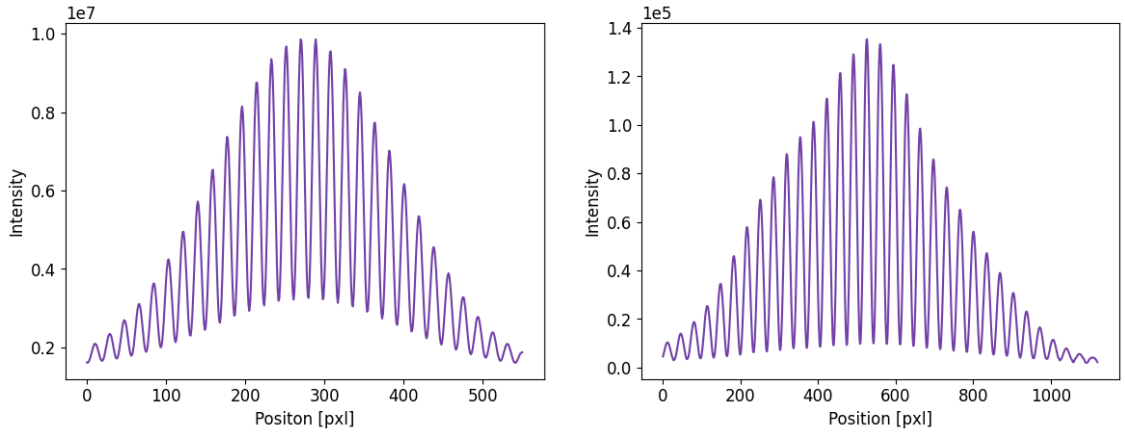

Figure 4.1: Example for data captured with the WinCamD (left) and the Mako camera (right). Shot at the same alignment and a time interval of a few minutes. The data from the Mako camera shows noticeable discrepencies from the ideal Gaussian shape.

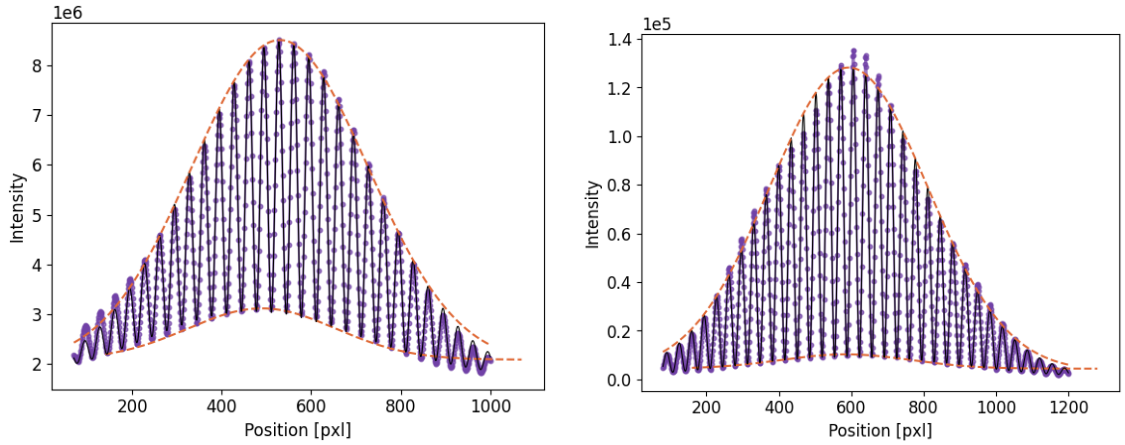

Figure 4.2: Example for fitcurves (black) applied to datapoints (purple) captured with the WinCamD (left) and the Mako camera (right), as well as the respective fits for the upper and lower envelope (orange). The data on the right corresponds to figure 4.1, while the WinCam data originates from a previous alignment.

Although the evaluated peaks originate only from the raw data analysis using the peakfinder, which is theoretically more error-prone than the fit, there is a high level of agreement between both methods. As shown in Figure 5.1, the second method has limited accuracy due to the pixel size of the camera, leading to a resolution of 0.2π. After a three-week Christmas break, the setup had to be completely realigned, and the aforementioned camera change took place, resulting in slight variations in these values. For the final setup, a fringe size of 202 µm in the imaging plane and a pixel size of 5.86 µm give a resolution of 0.18π. As the goal is to achieve a stabilization of about $\pm 0.1\pi$, this resolution is sufficient.
Consequently, the parameter selected for evaluation in the stabilization algorithm is the distance between the upper envelope center and the middle fringe, which only requires a fit of the envelope.

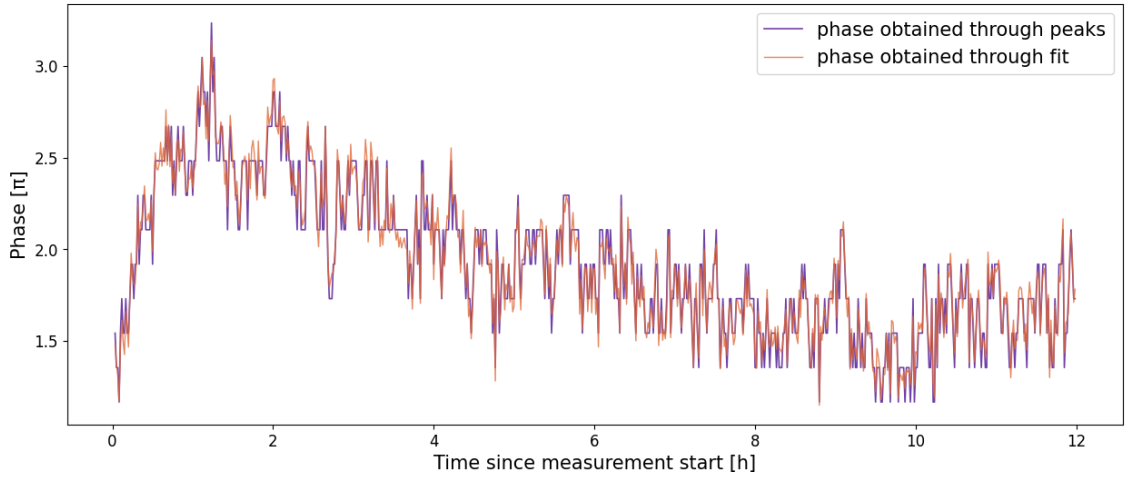

Figure 4.3: Comparison between the phase obtained by the fit (orange) and the phase calculated with a relative distance of the middle fringe (purple). The data originates from the measurement without stability in section 5.1.

4.2 Piezoelectric Feedback

Before the work on stabilization algorithm can begin, the response of the piezo stack and the effect on the accordion lattice need to be quantified. This was done for both configurations, before and after the camera switch.
The function-generator is set to a triangular signal with a peak to peak voltage of 0.4 V. As in all later measurements, the amplification of the analogue power amplifier is set to maximum, corresponding to a $\times 30$ amplification. The measured responses of the phase for both setups are depicted in figure 4.5, with identical

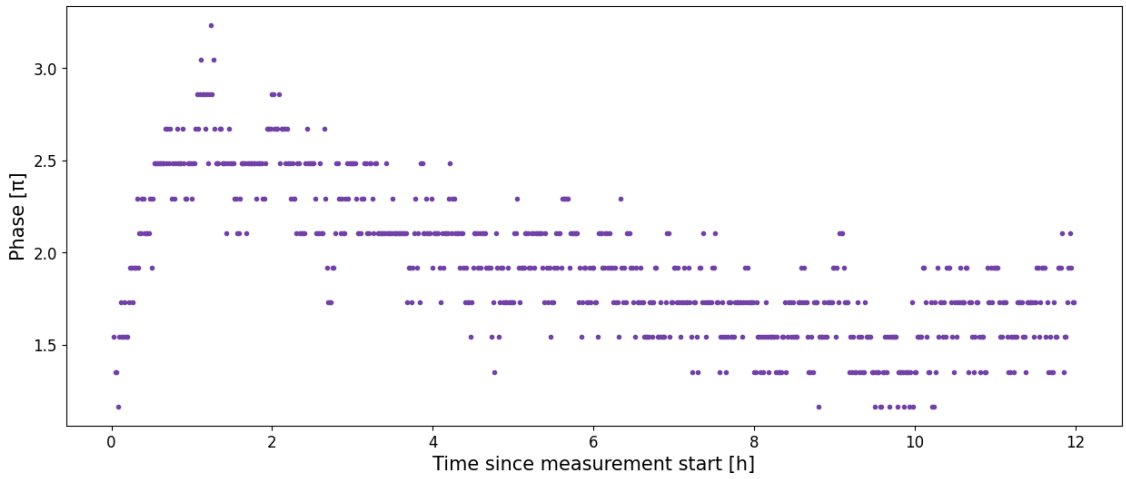

Figure 4.4: Resolution of the phase calculated with the peaks. The data originates from the measurement without stability in section 5.1.

parameters apart from a varied frequency.
Both measurements clearly reflect the applied triangular voltage, although the data from the mako camera (figure 4.5b) again shows large inaccuracies.
For this setup, the information obtained from the peaks shows a phase shift of $\Delta\varphi = 1.05\pi$, with a movement of the center fringe of 105.5 µm in the imaging plane or 2.38 µm in the trapping plane. This results in a conversion rate of 263.7 µm/V or 2.61 π/V.
Using this information it is also possible to determine the fringe distance by calculating the distance moved for a shift of $\Delta\varphi = 2\pi$. This gives d = 200.9 µm, which agrees excellently with the fringe distance of 201.8 µm determined through fitting.

Although these values match very well, a movement of the upper envelope was observed after a poorer match in the first setup. It is visible in figure 4.6 and was also found identically in the final setup.
Ideally, the motion of the piezo should be exactly parallel to the beam propagation direction, thus only changing the path length and not the beams direction. However, the stack was not optimally glued due to problems with the selected adhesive [10], and due to observated deviations during the alignment procedure, a slight bending of the mirror was considered to be probable.
This leads to errors in our assumption, and therefore to the observable undesired movement.
As the stabilization of the accordion lattice relies on evaluating the relative posi-

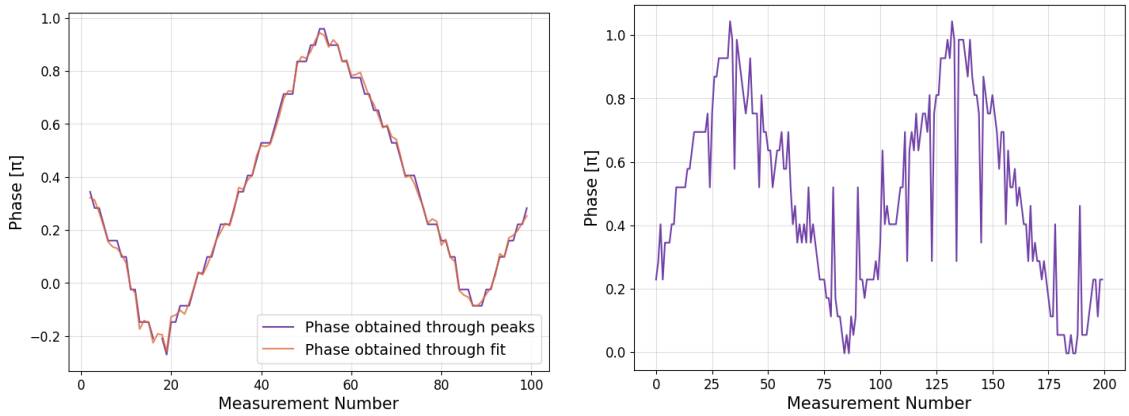

(a) Piezo response in first setup.

(b) Piezo response in final setup.

Figure 4.5: Response of the phase to a triangular voltage with $V_{pp} = 0.4\,\mathrm{V}$ applied to the piezo.

tion between the peak and the envelope, this motion inevitably impacts the performance of the mechanism. Regarding the peak's motion, the envelope shows a relative shift of 19.9%, a margin considered tolerable for stabilization within the experimental framework, given the minor nature of these adjustments.
Additionally, novel mounting of the piezo, planned in parallel to this thesis, is expected to improve the performance.

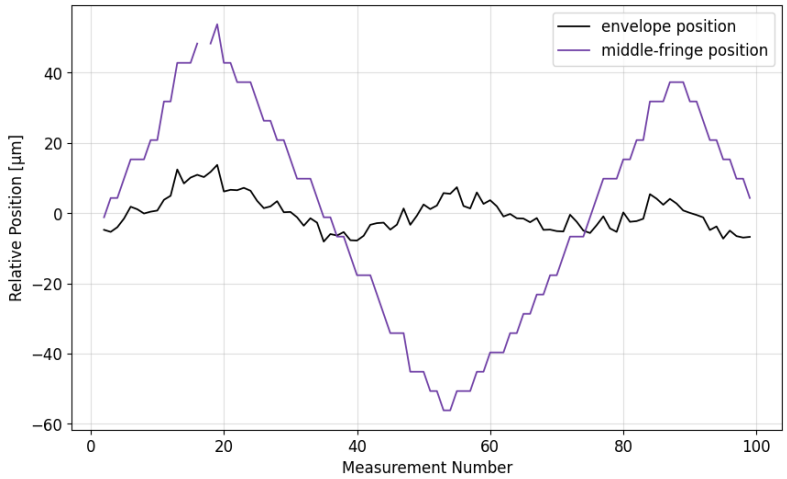

Figure 4.6: Movement of the envelope center and the middle fringe as a reaction to a triangular voltage applied to the piezo. One false measurement was removed from the fringe data.

4.3 Feedback Algorithm

The basic concept of the stabilization algorithm consists of taking an image in a fixed time interval, checking if correction is required and if so, applying a voltage.

Taking Data

Because the images from the Mako camera show some noticeable fluctuations (see figure 4.5b and section 4.1.1), and the acquired data must be very precise, the data acquisition process involves taking more than a single image. A number of around ten images (refer to section 5.2) are captured in succession, each of which is analysed separately, resulting in multiple values for the relative distance.

Processing the Data

To process the aforementioned dataset, the first step is to fit the Gaussian envelope for each image and determine the distance of its center and the middle fringe, as described in section 4.1.2. Subsequently, the calculated values are used to inspect for spurious measurements through the calculation of the standard deviation σ and subsequent removal of all measurements exhibiting deviations from the mean exceeding 2σ. The mean and standard deviation of the remaining values are then returned. Afterwards the resulting standard deviation is checked and if it is above a limit of 1 µm, the measurement is repeated.

Correction

If the mean distance surpasses the predefined threshold (see section 5.2), the program triggers a correction process. Utilizing the established conversion factor (as discussed in section 4.2), the mean distance is employed to compute the necessary voltage for its elimination. If the resulting voltage falls within the accepted boundary, it is added to the current DC-offset of the function generator, else the program rises an error message and shifts the lattice 2π in the opposite direction. Since the limit lies at $\pm 3\,\mathrm{V}$, which would correspond to a phase shift of 7.83π, this scenario is very improbable under a controlled environment.
Afterwards, a follow-up measurement is conducted to verify the success of the correction. If necessary, up to ten additional corrections will be performed to attain alignment within the designated threshold.
Upon successful correction, a fixed duration, called sleeptime, is waited before

initiating the entire process anew. A detailed experimental characterization of the stabilization loop and the involved parameters will be discussed in section 5.

5 Results

The following section will present the results of the effort for phase stabilization of the accordion lattice tap, including a brief overview over the chosen feedback parameters and their impact, as well as a reference measurement to quantify the long term drifts.

5.1 Initial Stability

In order to be able to precisely evaluate the stabilization, the phase drift of the setup without optimized stability is first investigated. Since the path difference of the beams is in the order of the light wavelength, the phase of the accordion lattice is very sensitive and even minor external disturbances have a noticeable effect on the stability. Therefore, a reliable measurement was not possible during the day due to other people working on the lab bench. To assess the stability, images were taken every minute over 12 hours during the night. The data can be seen in figure 4.3.
A phase shift of $\sim 0.6\pi$ is observed here, which would result in a loss of trap depth of 2,75% or 2.21 µK. Furthermore, the central fringe would experience a displacement of 5.81 µm, which, given the fringe size of 20 µm, would lead to a loss of atoms to the neighbouring fringe during the loading of the $\sim$ 15 µm sized atom cloud.

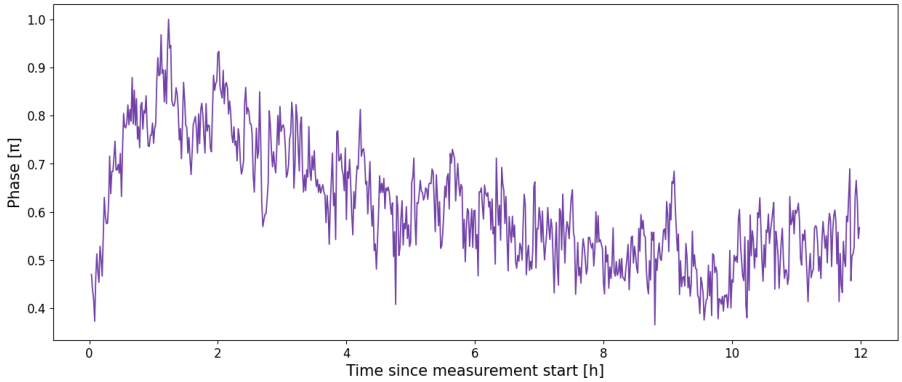

Figure 5.1: Measured phase over 12 hours during the night without stabilization.

5.2 Parameter Optimization Process

As discussed in section 4.3, the algorithmic feedback loop uses multiple predefined parameters during the stabilization process, for which additional testing and fine tuning is necessary.

Threshold

The threshold defines the trigger value of fringe displacement for initiating the correction process, thereby only correcting distance measurements above the threshold. This parameter thus determines the sensitivity of the stabilization.
In order to choose reasonable parameters here, the effect on the experimental context must be considered. To achieve a maximal fringe displacement of 1 µm during loading, a phase fluctuation of less than 0.1π is required. This would result in a maximum trap depth loss of 0.08% or 0.06 µK, which is more than sufficient for this experimental frame. After compression to the minimal fringe distance of 1.7 µm, this corresponds to a fringe displacement of 0.09 µm and a trap depth loss of 0.009% or 0.007 µK.
This shows, that the critical value is primarily the displacement while loading, which would be sufficient at 1 µm, but an even lower value would be ideal to minimize atom loss even further.
First, measurements were therefore carried out with a threshold of 0.04π, which would limit the displacement to 0.39 µm. However, the measurement shown in figure 5.2 reveals the problem of a too narrow threshold. Since the corrections are not always ideal, which might be due to inconsistencies in the response of the piezo to the applied voltage (see section 5.2), a small threshold often requires a re-correction. As observed at around 18:30 during the measurement of figure 5.2, this can lead to jumping back and forth around the correction limits in the case of successive overcorrections (too much voltage applied).
In order to keep the number of required corrections low and to avoid these instabilities, it was ultimately decided to discard a more precise restriction and to select a threshold of 0.1π.

Voltage Conversion Factor

The relationship between the voltage applied to the piezo stack and the achieved shift of the center fringe is described by the voltage conversion factor. In section 4.2 a factor of 263.7 µm/V was measured.

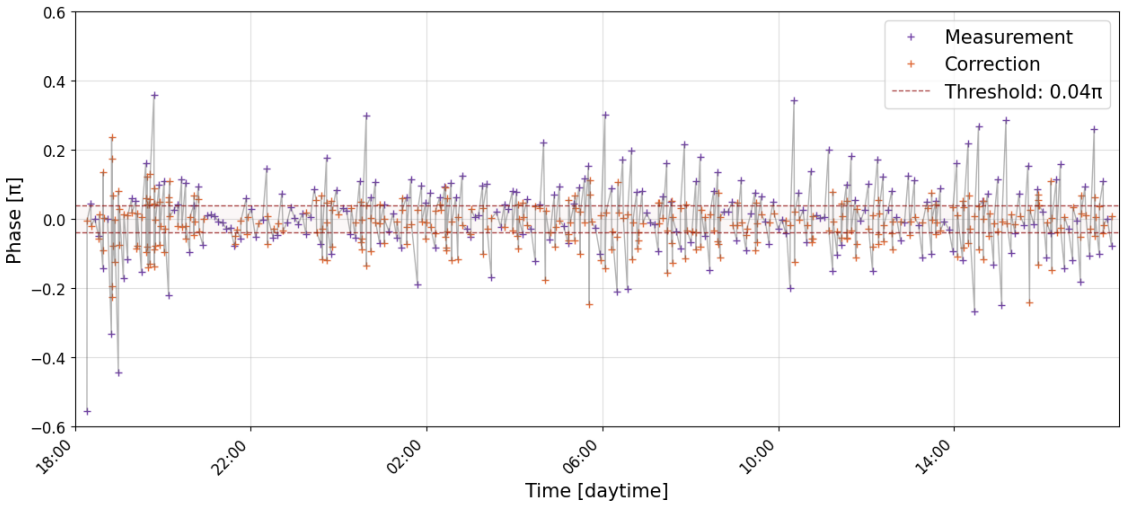

Figure 5.2: Exemplary stabilization measurement with a threshold of 0.04π. Plotted here is the measured phase, where the purple points represent standard measurements and the orange points the measurements to verify a conducted correction. The other parameters were: voltage conversion factor - 280 µm/V, sleeptime - 5 min, number of images - 10.

However, the first stabilization measurements showed that the values corrected with this factor often missed the target of an eliminated displacement. At times, they overshoot the envelope center, while at other times, they fall short of it. The calculated values for the conversion factor, derived from these responses to the applied voltage, differ significantly from the previously measured one. As shown in 5.3, very large fluctuations can be observed in both directions, leading to a standard deviation of 173.1 µm/V. Also observable here are multiple negative values, which would indicate a fringe movement opposite to the anticipated direction. These could originate from a massive overcorrection, inducing a phase more than π, which would lead to a change of reference fringe, since the neighbouring fringe is now closer to the envelope center. The algorithm is not capable of detecting this scenario, therefore making it a potential error source and emphasizing the importance of a well-isolated environment. As another possible reason of the negative values is simply an externally induced shift in between the correction and the follow-up measurement, a reliable correction of the thereby potentially falsified values is difficult. Compared to these fluctuations, the mean of 286.8 µm/V still agrees quite well with the expected value of 263.7 µm/V.
This implies that the problem is not a misestimation of the factor, but rather other irregularities like the reactions of the piezo. That inconsistency is a major source of error and often leads to the necessity for several corrections.

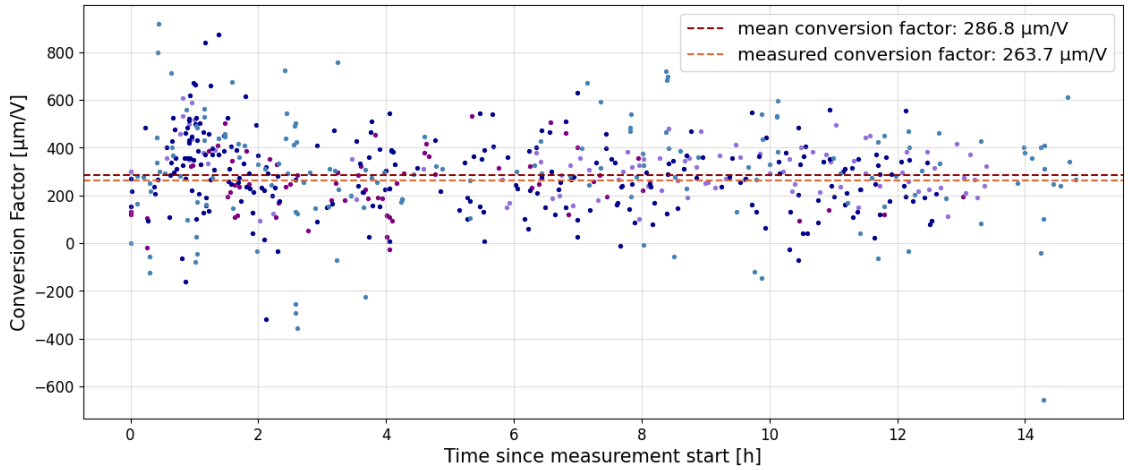

Figure 5.3: Calculated conversion factors using the measured distance before and after the correction as well as the applied voltage. The different colours indicate four different stabilization cycles with slightly different parameters, which are not relevant for the calculation.

One attempt to minimize these deviations consisted of selecting a fixed position instead of the center of the envelope as a reference for stabilization. The undesired movement of the envelope identified in section 4.2 thus no longer plays a role. Since the result shown in figure 5.4 with a standard deviation of 229.2 µm/V does not show any improvements, this can be eliminated as a potential cause.

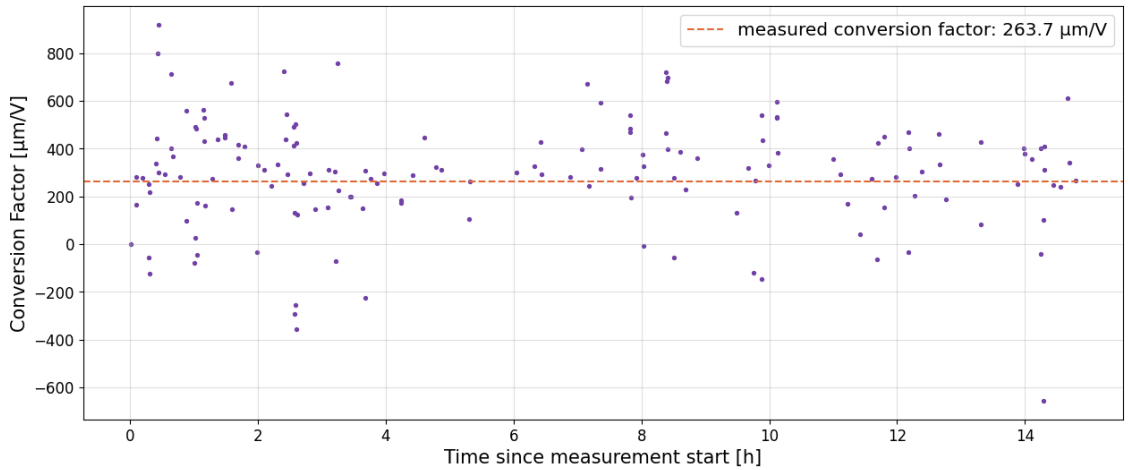

Figure 5.4: Calculated conversion factor as in figure 5.3 during stabilization to a fixed reference point.

A more application-oriented investigation of the piezo reaction is then conducted. The relative distance directly before and directly after a voltage jump of 0.03 V is

measured ten times in total with ten measurements in between at a constant voltage. The result can be seen in 5.5 and confirms the volatility of the piezo response and shows that the measurements are very jumpy overall.

In order to deal with these fluctuations in the best possible way, it was decided to set the factor to 300 µm/V, moderately above the measured value. This prevents the observed effect of bouncing back and forth around the correction limit due to overreaction. The more frequent error is then undercorrection, often necessitating only one additional corrective adjustment.

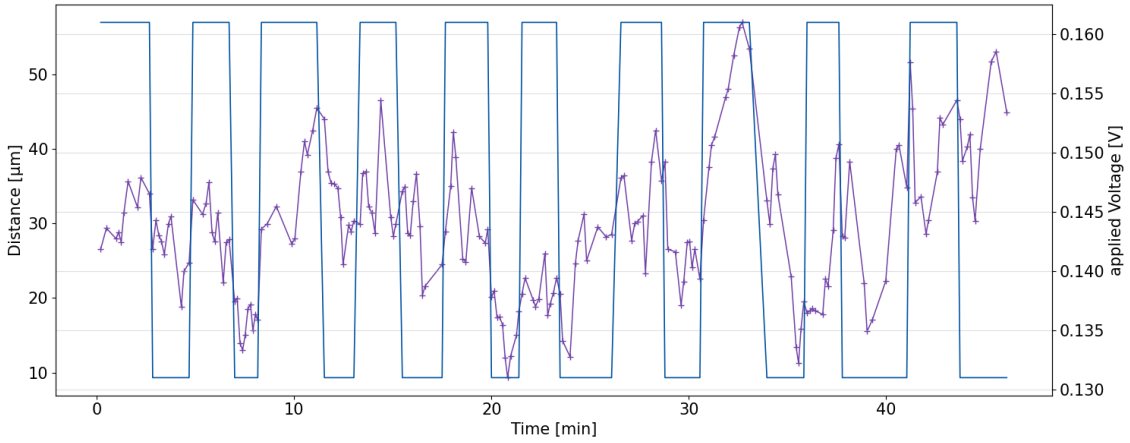

Figure 5.5: Measurement of the fringe displacement (purple) during ten voltage jumps of 0.03 V (blue) for piezo response characterization.

Sleeptime

The sleeptime defines the interval between two measurements, therefore determining the measurement frequency. Since the setup is highly sensitive and measurements have shown minor abrupt jumps, a value of a few minutes seems appropriate. A comparison of measurements with sleeptime durations of 5 minutes and 2 minutes reveals slight advantages of the shorter duration. However, as the differences are marginal and the primary task of stabilization is to prevent long-term drifts on the order of hours, further reduction is not particularly beneficial. Therefore, a value between 2 and 5 minutes is recommended. For the final parameterization of this work, a sleeptime of 2 minutes was chosen, considering the limited duration of measurements confined to nighttime.

Number of Images

In order to account for the imprecisions observed in the data from the Mako camera, each measurement consist of multiple images. A large number of images per measurement increases the precision, as the extracted mean is more accurate and the identification of false measurements is more reliable. However, each image must be fitted and calculated individually, which results in a significantly longer measurement time.
The compromise chosen is to take 10 images per measurement, as a reliable calculation of the average and the standard deviation is still possible and the measurement time remains in the lower second range. The average error per measurement in this case is $\sim 0.005\pi$ or $\sim 0.5\,\mu m$.
Stabilization with 20 images per measurement also show hardly any visible improvements during the process compared to the 10-image case, the calculated improvement of the error is in the order of 0.0001π and therefore likely only noise fluctuation.

Overview

An overview of the final parameter choices is depicted in table 5.1.

Threshold	Conversion Factor	Sleeptime	Number of Images
10 µm	300 µm/V	2 min	10

Table 5.1: Final parameters for the phase stabilization feedback loop.

5.3 Final Stabilization

Utilizing the final parameters outlined in section 5.2, this section focuses on a comprehensive performance analysis of the phase stabilization mechanism applied to the accordion lattice. Two measurements conducted during nighttime employing these parameters are illustrated in figure 5.6 and 5.7, serving as the foundation for subsequent analysis and discussion of the obtained results.

First, the maximal phase deviation that can be observed is 0.56π at around midnight in figure 5.6.
The corresponding voltage applied to the piezo during this measurement also

shows a sudden decline of $\sim 0.6\pi$ at that time. As the voltage afterwards stays at that level, a change of evaluated reference fringe (see section 5.2) due to some measurement error or external influence, is strongly indicated.
In the future application a much more controlled and protected environment will most likely minimize external influences and therefore those occurrences.
Apart from this outlier, both voltage curves reflect good responses to the long term phase drifts. Especially in figure 5.6, a clean suppression of a long term drift is visible after midnight.

Overall, the standard deviation of the measured points across both measurements amounts to 0.085π and is therefore slightly below the threshold 0.1π. This corresponds to an average center fringe displacement of 0.83 µm during the loading process. With the atom cloud size of $\sim$ 15 µm and the fringe distance of 20 µm, this movement is tolerable given a precisely aligned loading setup. The loss of trap depth amounts to only 0.056% or 0.045 µK.
For the corrected values, the standard deviation amounts to 0.054π, which is as expected quite high, considering the conversion factor analysis in section 5.2.
It also shows, that a stabilization with a confinement below 0.05π is difficult to realise. While using a finer threshold allows averaging lower displacements, the risk of causing successive overcorrections increasing.
For later implementation, the advantages of a precise average confinement have to be weighed against the potential of short term instabilities. A threshold between 0.1-0.05π is advised.

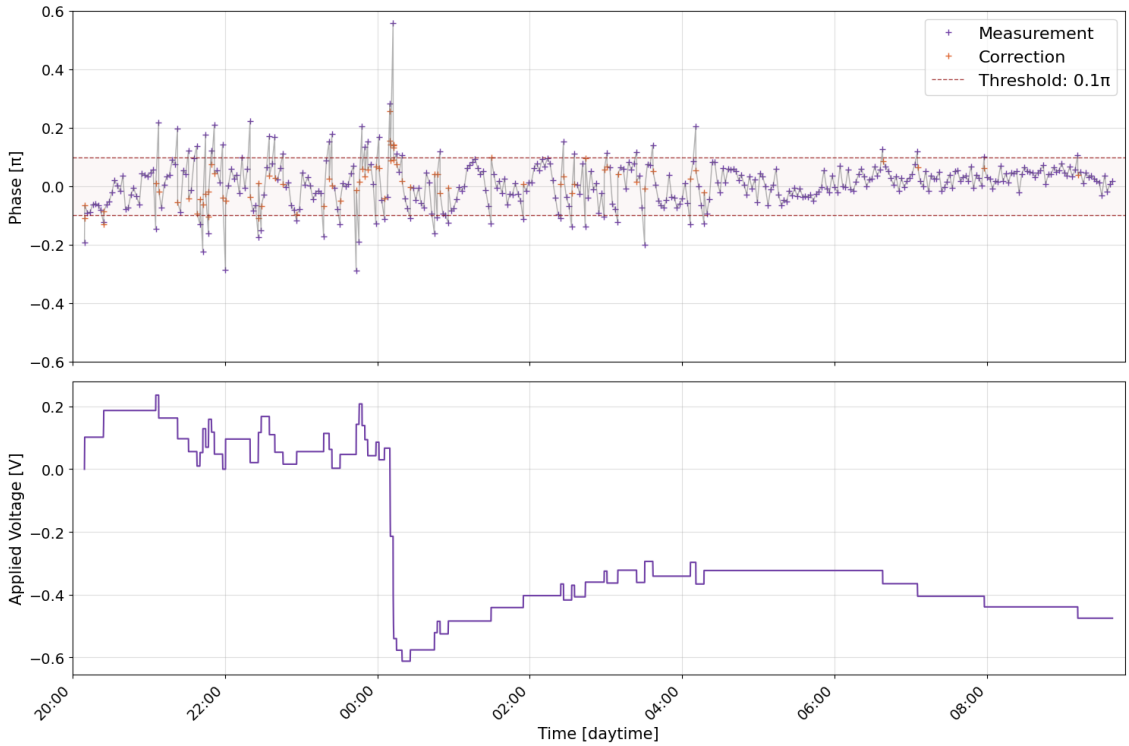

Figure 5.6: First measurement of the phase (top) and the applied voltage (bottom) during stabilization using the final parameters.

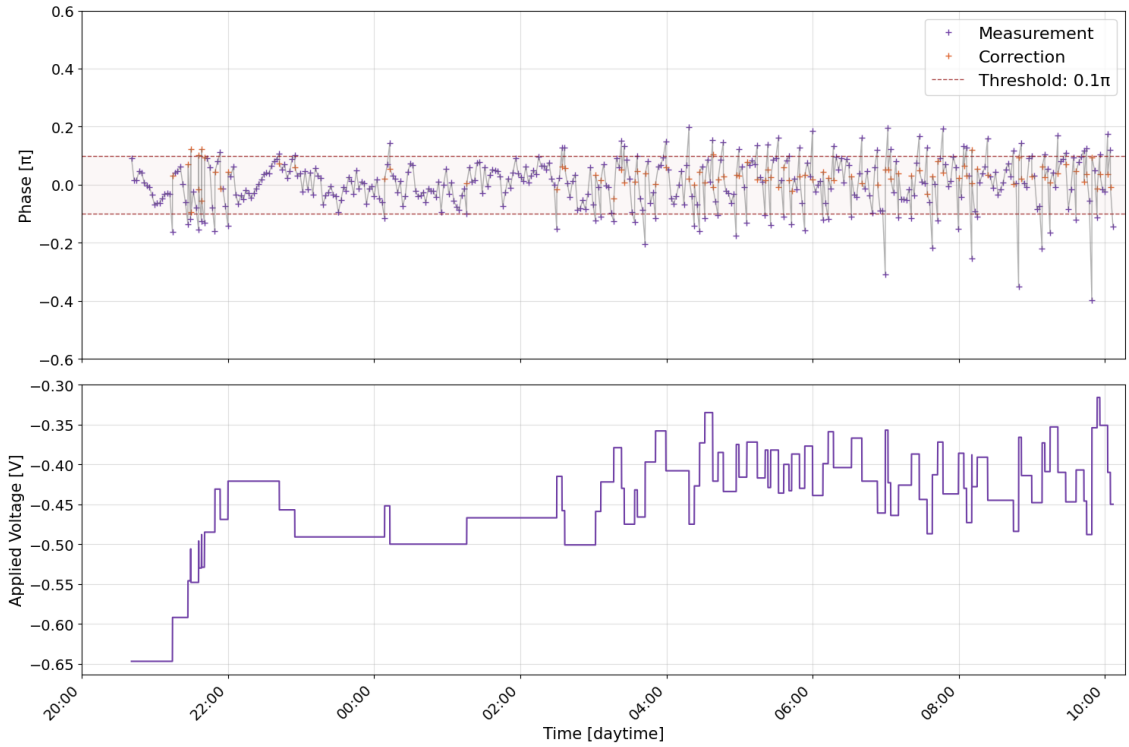

Figure 5.7: Second measurement of the phase (top) and the applied voltage (bottom) during stabilization using the final parameters.

6 Conclusion and Outlook

In this thesis, the stability of an accordion lattice dipole trap was improved by implementing an imaging setup in combination with a phase correction feedback algorithm.
The first step was reconstructing the existing accordion lattice design, serving as a test setup. Subsequent advancements included the incorporation of an imaging setup, necessitating the addition of two lenses and the development of an alignment procedure, as well as an objective lens and a camera. Despite encountering challenges such as inaccuracies after a camera switch and errors during measurements with the new camera, the captured images showed precise alignment and allowed to reliably extract the phase. The phase extraction was conducted by determining the relative shift of the captured middle fringe to the fitted center of the upper envelope.

After verifying the need for stabilization through the measurement of long-term passive phase drifts of $\sim 0.6\pi$, a piezo control setup was implemented, comprised of a piezoelectric conductor mounted to a reflecting mirror, a function generator and an analogue power amplifier. To manipulate the phase and thereby the position of the center fringe relative to the envelope center, a voltage was applied to the piezo, which by its movement manipulates the path difference between the interfering beams. Response measurements demonstrated the functionality and yielded a voltage to fringe movement conversion factor of 263.7 µm/V in the imaging plane of the test setup.
During the final stage, a feedback algorithm was developed to automate the phase measurement as well as the check for necessary correction voltages and subsequent application. Parameters such as threshold and voltage conversion factor were analyzed and optimized to achieve optimal system performance. The culmination of these efforts resulted in an average phase deviation of 0.085π, corresponding to a center fringe displacement of 0.83 µm and a trap depth loss of 0.045 µK (compared to a total trap depth of 80.2 nK). The crucial value of fringe displacement during loading is thus below the minimum target of 1 µm and significantly reduces the shift induced by the long term drifts of ~ 5.8 µm.

Room for improvement lies in the accuracy of the conducted corrections. The corresponding standard deviation of 0.054π shows the limitation of this setup, since further reduced threshold values, attempting increased precision, can lead to instabilities. One reason for those fluctuations could be the measured irregularities in the piezo response, but also measurement errors or external influences, which are also reflected by a few large outliers.

However, it is anticipated that the transition to the better isolated main setup will mitigate such occurrences and together with the planned implementation of a new piezo mounting system, which is expected to enhance the consistency in piezo response, the developed system promises an achievement of even higher precision for correction and stabilization in the future.

List of Figures

List of Tables

Bibliography

[1] M. H. Anderson et al. "Observation of Bose-Einstein Condensation in a Dilute Atomic Vapor". In: *Science* 269.5221 (1995), pp. 198–201. DOI: 10.1126/science.269.5221.198. URL: https://www.science.org/doi/abs/10.1126/science.269.5221.198.

[2] K. B. Davis et al. "Bose-Einstein Condensation in a Gas of Sodium Atoms". In: *Phys. Rev. Lett.* 75 (22 Nov. 1995), pp. 3969–3973. DOI: 10.1103/PhysRevLett.75.3969. URL: https://link.aps.org/doi/10.1103/PhysRevLett.75.3969.

[3] W. Ketterle, D. S. Durfee, and D. M. Stamper-Kurn. *Making, probing and understanding Bose-Einstein condensates*. 1999. arXiv: cond-mat/9904034 [cond-mat].

[4] Chayma Bouazza. "Ultracold dysprosium gas in optical dipole traps : control of interactions between highly magnetic atoms". Theses. Université Paris sciences et lettres, May 2018. URL: https://theses.hal.science/tel-01886206.

[5] Shuwei Jin et al. "Two-dimensional magneto-optical trap of dysprosium atoms as a compact source for efficient loading of a narrow-line three-dimensional magneto-optical trap". In: *Phys. Rev. A* 108 (2 Aug. 2023), p. 023719. DOI: 10.1103/PhysRevA.108.023719. URL: https://link.aps.org/doi/10.1103/PhysRevA.108.023719.

[6] Jianshun Gao. *A first two-dimensional magneto-optical trap for dysprosium*. 2022.

[7] Joschka Schöner. *Magnetic-Field Setup for Magneto-Optical Trapping and Interaction Tuning in a Novel Dysprosium Quantum Gas Experiment*. 2022.

[8] Lennart Hoenen. *Fast, High Precision Low Noise Bipolar Power Supply for Magnetic Field Coils in Ultra-Cold Dysprosium Experiment*. 2022.

[9] Valentina Salaza Silva. *The Accordion Lattice: Towards Trapping of Dysprosium Ultracold Gases in Two Dimensions*. 2023.

[10] Charles Drevon. *Characterisation of an accordion lattice setup for a low-dimensional dipolar quantum gases experiment*. 2023.

[11] Sarah Philips. *Characterizing a High-Resolution Imaging System for the Dysprosium Experiment*. 2023.

[12] Rudolf Grimm, Matthias Weidemüller, and Yurii B. Ovchinnikov. *Optical dipole traps for neutral atoms*. 1999. arXiv: physics/9902072 [physics.atom-ph].

[13] T. C. Li et al. "Real-time control of the periodicity of a standing wave: an optical accordion". In: *Opt. Express* 16.8 (Apr. 2008), pp. 5465–5470. URL: https://opg.optica.org/oe/abstract.cfm?URI=oe-16-8-5465.

[14] C. Ravensbergen et al. "Accurate Determination of the Dynamical Polarizability of Dysprosium". In: *Physical Review Letters* 120.22 (May 2018). DOI: 10.1103/physrevlett.120.223001. URL: http://dx.doi.org/10.1103/PhysRevLett.120.223001.

[15] Matthias Schmitt. "A Self-bound Dilute Quantum Liquid of Dysprosium Atoms". PhD thesis. Universität Stuttgart, Germany, 2017.

[16] Matthias Wenzel. *A dysprosium quantum gas in highly controllable optical traps*. 2015.

[17] Thomas Maier. "Interactions in a Quantum Gas of Dysprosium Atoms". PhD thesis. Universität Stuttgart, Germany, 2015.

[18] Z. Hadzibabic and M. Köhl. "Chapter 4 - Low-Dimensional Atomic Bose Gases". In: *Ultracold Bosonic and Fermionic Gases*. Ed. by Kathryn Levin, Alexander L. Fetter, and Dan M. Stamper-Kurn. Vol. 5. Contemporary Concepts of Condensed Matter Science. Elsevier, 2012, pp. 95–120. DOI: https://doi.org/10.1016/B978-0-444-53857-4.00004-0. URL: https://www.sciencedirect.com/science/article/pii/B9780444538574000040.

[19] Andreas Kerkmann. "A novel Apparatus for Quantum Gas Microscopy of Lithium Atoms". PhD thesis. Universität Hamburg, 2019. URL: https://ediss.sub.uni-hamburg.de/handle/ediss/6115.

[20] Anne Herbert. "A dipolar erbium quantum gas microscope". PhD thesis. Harvard University Graduate School of Arts and Sciences, 2021. URL: https://nrs.harvard.edu/URN-3:HUL.INSTREPOS:37368261.

Acknowledgements - Danksagung

Finally, I would like to say thank you!

First to Lauriane Chomaz, for her great support during the last few months. Her ideas and suggestions were a vital part to the success of this project. I am so grateful to have had her as my supervisor.
Next to Jianshun Gao, who introduced me to the world of optics and was always there to help me combat upcoming complications.
Also to the rest of the YD-group, who made this time so much more enjoyable, I will definitely miss the card games after lunch.
Thank you to all my friends in Heidelberg for making my time studying here as great as it was. I will miss you.
And thanks to you Emma.
And while I'm at it, thanks to my parents, my second parents and my sister for being in my life.

Erklärung

Ich versichere, dass ich diese Arbeit selbstständig verfasst und keine anderen als die angegebenen Quellen und Hilfsmittel benutzt habe.

Heidelberg, den 28. Februar 2024